

# DCPI-Depth: Explicitly Infusing Dense Correspondence Prior to Unsupervised Monocular Depth Estimation

Mengtan Zhang<sup>1</sup>, Yi Feng<sup>1</sup>, Qijun Chen<sup>1</sup>, *Senior Member, IEEE*, and Rui Fan<sup>1</sup>, *Senior Member, IEEE*

**Abstract**—There has been a recent surge of interest in learning to perceive depth from monocular videos in an unsupervised fashion. A key challenge in this field is achieving robust and accurate depth estimation in challenging scenarios, particularly in regions with weak textures or where dynamic objects are present. This study makes three major contributions by delving deeply into dense correspondence priors to provide existing frameworks with explicit geometric constraints. The first novelty is a contextual-geometric depth consistency loss, which employs depth maps triangulated from dense correspondences based on estimated ego-motion to guide the learning of depth perception from contextual information, since explicitly triangulated depth maps capture accurate relative distances among pixels. The second novelty arises from the observation that there exists an explicit, deducible relationship between optical flow divergence and depth gradient. A differential property correlation loss is, therefore, designed to refine depth estimation with a specific emphasis on local variations. The third novelty is a bidirectional stream co-adjustment strategy that enhances the interaction between rigid and optical flows, encouraging the former towards more accurate correspondence and making the latter more adaptable across various scenarios under the static scene hypotheses. DCPI-Depth, a framework that incorporates all these innovative components and couples two bidirectional and collaborative streams, achieves state-of-the-art performance and generalizability across multiple public datasets, outperforming all existing prior arts. Specifically, it demonstrates accurate depth estimation in texture-less and dynamic regions, and shows more reasonable smoothness.

**Index Terms**—unsupervised, depth estimation, dynamic object, dense correspondence, geometric constraint.

## I. INTRODUCTION

**M**ONOCULAR depth estimation, a crucial research field in computer vision and robotics, has applications across various domains, such as autonomous driving [1], augmented reality [2], and embodied artificial intelligence [3]. It provides agents with powerful environmental perception capabilities, enabling robust ego-motion estimation and 3D geometry reconstruction [4]. Early monocular depth estimation approaches

[5]–[7], developed based on supervised learning, typically require a large amount of well-annotated, per-pixel depth ground truth (generally acquired using high-precision LiDARs) for model training [8], [9]. Nevertheless, collecting and labeling such data is tedious and costly [8], [10]. Thus, the practical use of these supervised approaches remains limited.

In recent years, un/self-supervised monocular depth estimation has garnered significant attention [4], [10]–[14]. Such approaches obviate the need for extensive depth ground truth by leveraging either stereo image pairs [15], [16] or monocular videos to jointly learn depth and ego-motion estimation [4]. Specifically, given the target and source images, the estimated depth map (at the target view) and camera ego-motion are employed to warp the source image into the target view. The depth estimation network (hereafter referred to as *DepthNet*) and the pose estimation network (hereafter referred to as *PoseNet*) are then jointly trained in an un/self-supervised manner by minimizing the photometric loss, which measures the consistency between the reconstructed and original target images [4], [10], [13].

Despite the progress made, three limitations in existing frameworks continue to impede further advances in monocular depth estimation:

- (1) DepthNet perceives depth based on the contextual information in RGB images. While it effectively determines whether an object is in front of or behind another, accurately and efficiently learning their relative distance by minimizing the photometric loss is challenging. This is because photometric loss cannot directly reflect the magnitude of depth error, sometimes resulting in unsuitable gradients for optimizing depth during backpropagation.
- (2) Local depth variation is commonly constrained by edge-aware smoothness loss, which encourages local smoothness in depth based on image gradients [15]. However, since changes in image intensity do not directly correlate with local depth variation, this enforced smoothing can introduce errors in depth estimation.
- (3) Comparable photometric losses can result from different rigid flows, which may map a pixel to the wrong candidates with similar pixel intensities. This implies that the supervisory signals provided by the photometric loss to DepthNet and PoseNet are indirect, possibly leading to unsatisfactory robustness of monocular depth estimation, particularly in regions with weak textures.

This research was supported by the Science and Technology Commission of Shanghai Municipal under Grant 22511104500, the National Natural Science Foundation of China under Grant 62233013, the Fundamental Research Funds for the Central Universities, and Xiaomi Young Talents Program. (Corresponding author: Rui Fan)

Mengtan Zhang, Yi Feng, Qijun Chen, and Rui Fan are with the College of Electronics & Information Engineering, Shanghai Research Institute for Intelligent Autonomous Systems, Shanghai Institute of Intelligent Science and Technology, the State Key Laboratory of Intelligent Autonomous Systems, and Frontiers Science Center for Intelligent Autonomous Systems, Tongji University, Shanghai 201804, China (e-mails: 2050026@tongji.edu.cn, fengyi@ieec.org, {qjchen, rfan}@tongji.edu.cn).

Therefore, in this article, we introduce a novel unsupervised monocular depth estimation framework, known as **Dense Correspondence Prior-Infused Depth (DCPI-Depth)**, to overcome the limitations above by exploiting the depth cues in dense correspondence priors. Our DCPI-Depth consists of two bidirectional and collaborative streams: a traditional photometric consistency-guided (PCG) stream and our proposed correspondence prior-guided (CPG) stream. The PCG stream, following the prevalently used methods [4], [10], [13], [14], employs estimated depth and ego-motion information to warp the source frame into the target view, and then computes a photometric loss to provide the supervisory signal. On the other hand, the CPG stream leverages a pre-trained FlowNet [17] to provide dense correspondence priors. These priors are first utilized along with the estimated ego-motion to construct a geometric-based depth map via triangulation [18]. Such an explicitly derived depth map captures accurate relative distances among pixels. By enforcing consistency between these two sources of depth maps through a newly developed contextual-geometric depth consistency (CGDC) loss, we significantly optimize the convergence of DepthNet during training. Moreover, optical flow divergence, a differential property of dense correspondence priors, is found to have an explicit relationship with depth gradient. Building upon this relationship, we develop a novel differential property correlation (DPC) loss to improve depth quality from the aspect of local variation. Finally, a bidirectional stream co-adjustment (BSCA) strategy is adopted to make the two streams complement each other, where the rigid flow in the PCG stream mainly alleviates the misguidance of the CPG stream to depth on dynamic objects, while the optical flow in the CPG stream refines the rigid flow of the PCG stream with dense correspondences.

In summary, the main contributions of this article include:

- DCPI-Depth, a novel unsupervised monocular depth estimation framework with a CPG stream developed to infuse dense correspondence prior into the traditional PCG stream;
- A CGDC loss to optimize the convergence of DepthNet using a geometric-based depth map constructed by triangulating dense correspondence priors with estimated ego-motion;
- A DPC loss to further refine the quality of the estimated depth from the aspect of local variation based on the explicit relationship between optical flow divergence and depth gradient;
- A BSCA strategy to enable the two streams to complement each other, with a specific emphasis on improving depth accuracy in dynamic regions without masking technique.

The remainder of this article is organized as follows: Sect. II presents an overview of the existing monocular depth estimation methods. In Sect. III, we detail the proposed DCPI-Depth framework. In Sect. IV, we present the experimental results across several public datasets. Finally, we conclude this article and discuss possible future work in Sect. V.

## II. RELATED WORK

### A. Supervised Monocular Depth Estimation

Supervised monocular depth estimation approaches require depth ground truth for model training. As the first attempt, the study [5] proposes a coarse-to-fine architecture and a scale-invariant loss function to perceive depth from a single image. Subsequent research focuses mainly on improving depth estimation performance by exploring more intricate network architectures [6], [7], [19] or developing new loss functions [20]–[22]. For example, in studies [19] and [22], monocular depth estimation was reformulated as a per-pixel classification task, where depth ranges instead of exact depth values are predicted. Furthermore, to combine the benefits of both regression and classification tasks, the study [23] redefines this problem as a per-pixel classification-regression task. In [24], multi-scale guidance layers are introduced to establish connections between intermediate-layer features and the final depth map. In [25], a vision Transformer (ViT)-based architecture was developed to capture long-range correlations in depth estimation. More recently, Depth Anything [26] has demonstrated impressive performance, primarily due to its powerful backbone (a ViT-based vision foundation model) that is capable of extracting general-purpose, informative deep features. It first reproduces a MiDaS-based [27] teacher model with pre-trained weights from DINOv2 [28], and then utilizes the teacher’s predictions as pseudo-labels to train a student model on large-scale unlabeled data. While these methods have shown promising results, the need for extensive ground-truth depth data for supervised model training imposes considerable costs, thus limiting their wider applicability, especially in autonomous driving. Therefore, un/self-supervised monocular depth estimation approaches require greater attention.

### B. Un/Self-Supervised Monocular Depth Estimation

To liberate monocular depth estimation from dependence on extensive ground-truth data, un/self-supervised approaches [4], [10], [13]–[15] have emerged as visible alternatives. These methods typically utilize estimated depth to establish a differentiable warping between two images and employ photometric loss as the supervisory signal [4], [29]. The study [29] represents the first reported attempt to learn monocular depth estimation from stereo image pairs within a self-supervised framework. Subsequently, the study [4] extends this approach by coupling the learning of depth and ego-motion estimation from monocular videos. However, un/self-supervised methods often face challenges with independently moving objects and preserving clear object boundaries, due to multi-view ambiguities [13]. Therefore, in [10], a minimum reprojection loss and an auto-masking technique were introduced to exclude such regions during model training, significantly improving depth estimation performance. Building upon these prior arts, several studies have explored more sophisticated network architectures [14], [30]–[35] for improved performance. Others have incorporated multi-task learning, such as optical flow estimation [36]–[38] and semantic segmentation [39], [40], to address the challenges with dynamic objects.

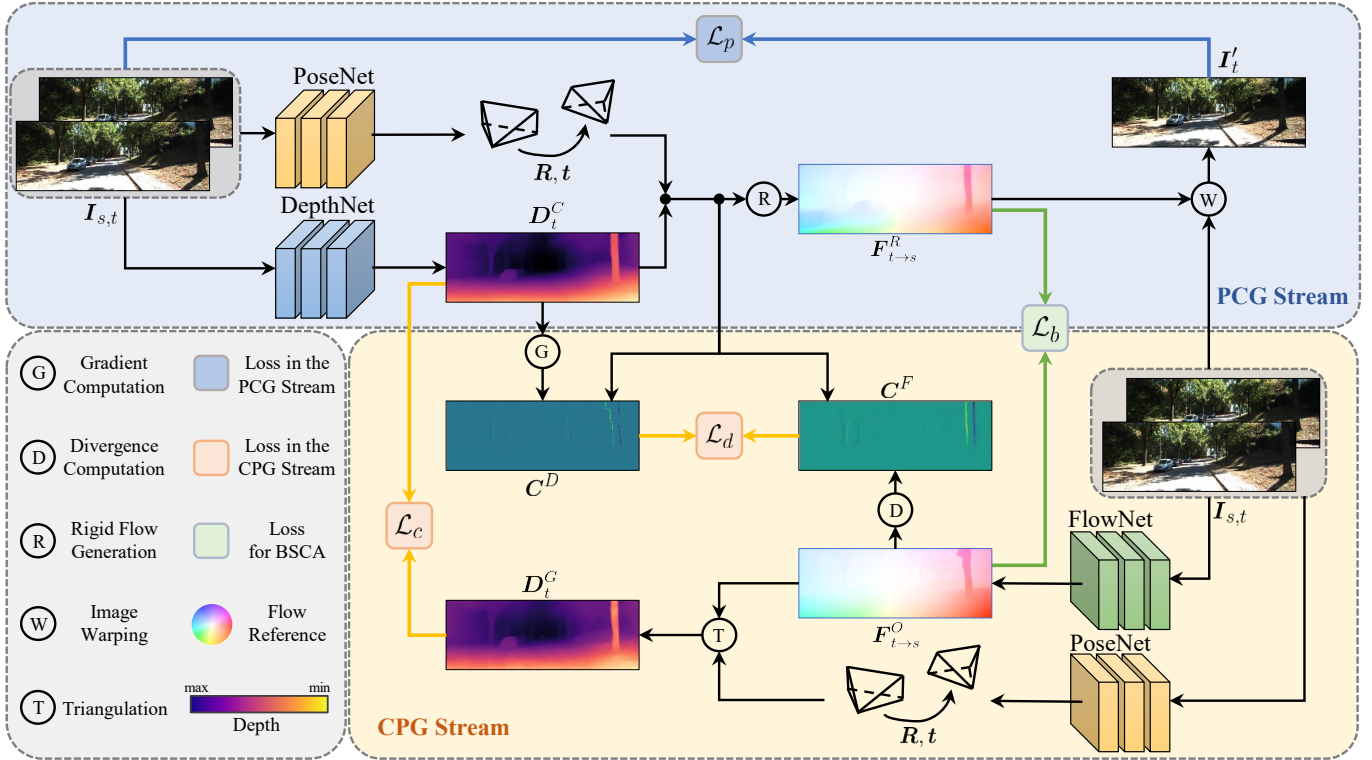


Fig. 1: The overall architecture of our proposed DCPI-Depth framework, which consists of two collaborative and bidirectional streams: PCG and CPG. The input image pairs, PoseNet, and the estimated ego-motion are depicted separately in each stream.

While these efforts have demonstrated promising performance, the existing unsupervised frameworks still present significant opportunities for refinement [13]. This limitation primarily arises from the reliance on contextual information to infer the pixel-wise depth map, which is indirectly supervised through the minimization of photometric loss. In the absence of guidance from additional and meaningful prior knowledge, DepthNet struggles to perform robustly in challenging scenarios. Therefore, in study [13], a monocular depth estimation model pre-trained on large-scale datasets is utilized to provide pseudo depth, a single-image depth prior, and two depth refinement loss functions are also designed to achieve more robust and reliable depth estimation. However, the limited accuracy of the pseudo depth significantly restricts the refinement capabilities of these loss functions. Therefore, in this article, we resort to dense correspondence priors for depth refinement. Unlike pseudo depth, these priors offer more direct, reliable, and interpretable geometric guidance through our developed CGDC and DPC losses.

### III. METHODOLOGY

#### A. Overall Architecture

As illustrated in Fig. 1, our proposed DCPI-Depth framework comprises two collaborative and bidirectional streams: PCG and CPG. The former, following the prior studies [10], [13], [14], effectively yet indirectly supervises the training of DepthNet and PoseNet through photometric loss, while the latter infuses dense correspondence priors (provided by a pre-trained FlowNet) into the former to overcome the limitations of

current SoTA frameworks [13], [14], [35], which rely solely on the PCG stream. Specifically, within the CPG stream, we introduce two novel loss functions: (1) a CGDC loss that guides the training of DepthNet by enforcing consistency between geometric-based and contextual-based depth maps, enabling DepthNet to capture accurate relative distances among pixels, thereby optimizing its convergence during training; (2) a DPC loss to constrain the local variation of depth based on the explicit relationship between optical flow divergence and depth gradient. Furthermore, we develop a BSCA strategy to collectively improve the aforementioned two streams: the rigid flow ensures accurate geometric guidance for depth estimation mainly on dynamic objects within the CPG stream, while the optical flow refines the rigid flow with dense correspondence within the PCG stream, thus allowing these two streams to effectively complement each other.

#### B. Contextual-Geometric Depth Consistency Loss

In the conventional PCG stream, given target and source video frames<sup>1</sup>  $I_{t,s} \in \mathbb{R}^{H \times W \times 3}$ , DepthNet takes  $I_t$  as input to infer a depth map  $D_t^C \in \mathbb{R}^{H \times W}$  based on contextual information, where  $H$  and  $W$  represent the height and width of the input image, respectively, while PoseNet estimates the ego-motion, including a rotation matrix  $R = [r_1^T, r_2^T, r_3^T]^T \in SO(3)$  and a translation vector  $t = [t_1, t_2, t_3]^T \in \mathbb{R}^3$  from the source view to the target view. The rigid flow map

<sup>1</sup>In this article, the subscripts “ $t$ ” and “ $s$ ” denote “target” and “source”, respectively.

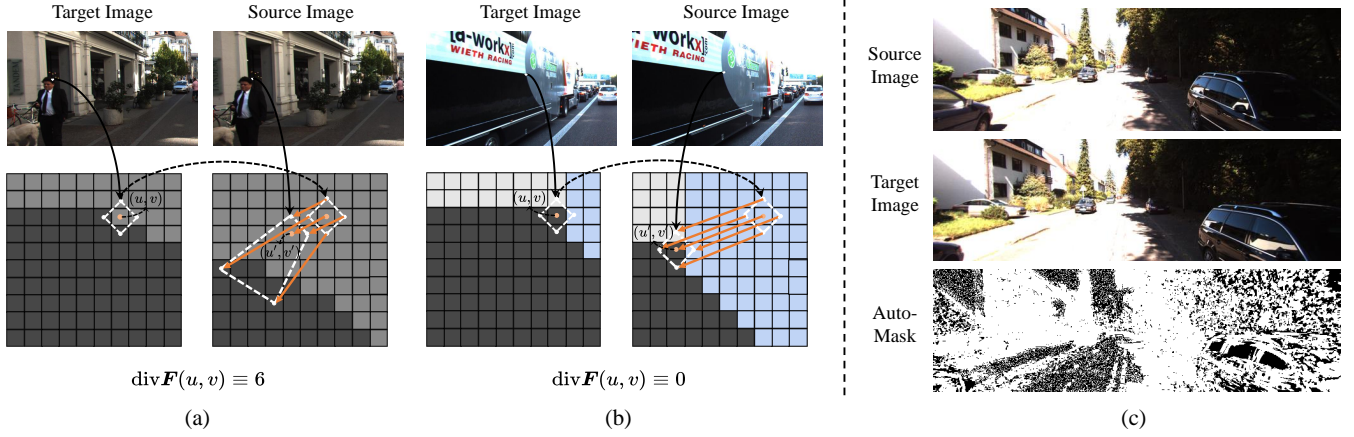


Fig. 2: Illustrations of optical flow divergence and auto-masking result: (a) optical flow divergence for pixels with similar intensities yet being spatially discontinuous; (b) optical flow divergence for pixels with significantly different intensities yet being spatially continuous; (c) auto-masking result for the given source and target images. A given pixel and its four neighbors in the target image are utilized for visualization in (a) and (b), where it can be observed that their correspondences in the source image are widely separated in (a) but similarly distributed in (b). The auto-masking algorithm tends to overly mask static regions, particularly in low-texture areas or when overexposed, and cannot effectively mask dynamic objects.

$\mathbf{F}_{t \rightarrow s}^R \in \mathbb{R}^{H \times W \times 2}$  from the target view to the source view can then be generated as follows:

$$\begin{bmatrix} \mathbf{F}_{t \rightarrow s}^R(\mathbf{p}_t) \\ 0 \end{bmatrix} + \tilde{\mathbf{p}}_t \sim \mathbf{K} \begin{bmatrix} \mathbf{R} & \mathbf{t} \\ \mathbf{D}_t^C(\mathbf{p}_t) \mathbf{K}^{-1} \tilde{\mathbf{p}}_t \\ 1 \end{bmatrix}, \quad (1)$$

where the symbol  $\sim$  indicates that two vectors are equal up to a scale factor,  $\mathbf{K}$  represents the camera intrinsic matrix,  $\mathbf{p}_t = [u, v]^\top$  denotes a 2D pixel, and  $\tilde{\mathbf{p}}_t$  is its homogeneous coordinates.  $\mathbf{I}_s$  is then warped into the target view using the rigid flow map  $\mathbf{F}_{t \rightarrow s}^R$ , generating  $\mathbf{I}'_t$ . By comparing  $\mathbf{I}'_t$  with  $\mathbf{I}_t$ , the following photometric loss is computed to provide a supervisory signal for the training of both DepthNet and PoseNet [41]:

$$\mathcal{L}_p = \alpha \frac{1 - SSIM(\mathbf{I}'_t, \mathbf{I}_t)}{2} + (1 - \alpha) \|\mathbf{I}'_t - \mathbf{I}_t\|_1, \quad (2)$$

where  $SSIM$  denotes the pixel-wise structural similarity index operation [42], and  $\alpha$  is an empirical weight set to 0.85.

DepthNet in the conventional PCG stream is trained to infer depth value per pixel from contextual information by minimizing (2) based on given RGB image pairs. Previous studies have neglected to incorporate geometric guidance into DepthNet training, leading to a significant limitation. While DepthNet can ascertain whether an object is in front of or behind another relative to the camera origin from contextual information, it struggles to effectively learn the extent of their relative distances solely by minimizing the photometric loss. This challenge arises because errors in image intensities do not directly reflect depth errors in terms of magnitude, rendering the gradient from photometric loss during back-propagation not always suitable for depth optimization.

To address these limitations, we resort to dense correspondence priors to generate another depth map based on well-developed and interpretable principles of multi-view geometry, thereby providing an additional constraint on depth estimation from RGB images. We first introduce a pre-trained FlowNet

[17] to generate the optical flow map  $\mathbf{F}_{t \rightarrow s}^O \in \mathbb{R}^{H \times W \times 2}$ , from which the following dense correspondence priors are derived:

$$\begin{cases} \hat{\mathbf{p}}_t^C = \mathbf{K}^{-1} \tilde{\mathbf{p}}_t \\ \hat{\mathbf{p}}_s^C = \mathbf{K}^{-1} \left( \tilde{\mathbf{p}}_t + \begin{bmatrix} \mathbf{F}_{t \rightarrow s}^O(\mathbf{p}_t) \\ 0 \end{bmatrix} \right), \end{cases} \quad (3)$$

where  $\hat{\mathbf{p}}_t^C$  and  $\hat{\mathbf{p}}_s^C$  represent a pair of normalized camera coordinates along the optical axis in the target and the source views, respectively. We then leverage such dense correspondence priors along with the ego-motion estimated by PoseNet to construct a geometric-based depth map  $\mathbf{D}_t^G \in \mathbb{R}^{H \times W}$  via triangulation [18] based on the following relationship:

$$\hat{\mathbf{p}}_s^C \sim \begin{bmatrix} \mathbf{R} & \mathbf{t} \\ \mathbf{D}_t^G(\mathbf{p}_t) \hat{\mathbf{p}}_t^C \\ 1 \end{bmatrix}. \quad (4)$$

$\hat{p}_{s,i}^C$ , the  $i$ -th element in  $\hat{\mathbf{p}}_s^C$  ( $i = \{1, 2\}$ ), is expressed as follows:

$$\hat{p}_{s,i}^C = \frac{\mathbf{D}_t^G(\mathbf{p}_t) \mathbf{r}_i^\top \hat{\mathbf{p}}_t^C + t_i}{\mathbf{D}_t^G(\mathbf{p}_t) \mathbf{r}_3^\top \hat{\mathbf{p}}_t^C + t_3}. \quad (5)$$

$\mathbf{D}_t^G$  can then be yielded as follows:

$$\mathbf{D}_t^G(\mathbf{p}_t) = \frac{\sum_{i=1}^2 (t_i - \hat{p}_{s,i}^C t_3)}{\sum_{i=1}^2 (\hat{p}_{s,i}^C \mathbf{r}_3^\top \hat{\mathbf{p}}_t^C - \mathbf{r}_i^\top \hat{\mathbf{p}}_t^C)}. \quad (6)$$

Finally, we employ the following CGDC loss:

$$\mathcal{L}_c = \frac{1}{HW} \sum_{\mathbf{p}} \left| \frac{\mathbf{D}_t^G(\mathbf{p}) - \mathbf{D}_t^C(\mathbf{p})}{\mathbf{D}_t^C(\mathbf{p})} \right| \quad (7)$$

to provide DepthNet with an additional constraint, enabling it to capture accurate relative distances among pixels. Considering that higher depth values potentially exhibit greater

absolute depth error, we adopt relative error in our CGDC loss to ensure more consistent gradients for back-propagation across all pixels. The effectiveness of our proposed CGDC loss is validated and discussed in Sect. IV-E.

### C. Differential Property Correlation Loss

Existing approaches [14], [35] that include only the PCG stream often struggle to distinguish and effectively handle regions with different levels of continuity. Specifically, these methods encounter difficulties in ensuring smooth depth changes in continuous regions and preserving clear boundaries near or at discontinuities. This problem arises primarily due to the lack of proper constraints that encourage DepthNet to consider local depth variations, especially since the depth of each pixel is estimated independently. Several studies [8], [10], [14], [35], [41], [43] introduced an edge-aware smoothness loss based on image gradients, initially presented in [15], to encourage local smoothness in depth estimation. However, such a loss function is somewhat problematic and incomplete. While this loss function is effective in regions where depth and image intensity have consistent change trends, it cannot constrain the extent of smoothing. Moreover, in continuous regions with rich texture or at discontinuities with subtle texture changes, this loss function may prove ineffective or even cause misleading guidance.

Compared to pixel intensity, it has been found that the dense correspondence priors between two images, as provided by FlowNet, have a more direct relationship with depth changes. As illustrated in Fig. 2(a), adjacent pixels that have similar intensities but are spatially discontinuous (because they are located on different objects) are likely to exhibit significantly different apparent motions, resulting in high optical flow divergence due to the separation of these pixels. In contrast, as illustrated in Fig. 2(b), pixels that have different intensities but are located in continuous regions typically have similar apparent motions, resulting in low optical flow divergence.  $\text{div}\mathbf{F}$ , the divergence of the given optical flow  $\mathbf{F}$  can be numerically calculated through the following expression:

$$\text{div}\mathbf{F}(u, v) \equiv -\mathbf{n}_u^\top \mathbf{F}(u-1, v) + \mathbf{n}_u^\top \mathbf{F}(u+1, v) \quad (8)$$

$$+ \mathbf{n}_v^\top \mathbf{F}(u, v+1) - \mathbf{n}_v^\top \mathbf{F}(u, v-1),$$

where  $\mathbf{n}_u = [1, 0]^\top$  and  $\mathbf{n}_v = [0, 1]^\top$  are two unit vectors in the horizontal and vertical directions, and  $\equiv$  represents discretization. Therefore, we establish an explicit constraint on local depth variation by leveraging the two correlated differential properties: optical flow divergence and depth gradient. This allows for more accurate depth estimation by ensuring that changes in depth are consistently aligned with variations in optical flow. It has been proven in the study [44] that rotational flow is independent of depth. Therefore, only the translational component of ego-motion contributes to constraining depth estimation from the aspect of local variation using optical flow divergence, and incorporating rotational flow, particularly when it is substantial, can disrupt this constraint. To address this issue, we eliminate the rotational apparent motions in the optical flow using the following expression:

$${}^t\mathbf{F}_{t \rightarrow s}^O = \mathbf{F}_{t \rightarrow s}^O - {}^R\mathbf{F}_{t \rightarrow s}^R, \quad (9)$$

where  ${}^t\mathbf{F}_{t \rightarrow s}^O$  denotes the translational optical flow, and  ${}^R\mathbf{F}_{t \rightarrow s}^R$ , the rotational rigid flow, is generated using the estimated  $\mathbf{R}$  and a translation vector of zeros  $\mathbf{0}$  as follows:

$$\begin{bmatrix} {}^R\mathbf{F}_{t \rightarrow s}^R(\mathbf{p}_t) \\ \mathbf{0} \end{bmatrix} + \tilde{\mathbf{p}}_t \sim \mathbf{K} \begin{bmatrix} \mathbf{R} & \mathbf{0} \end{bmatrix} \begin{bmatrix} \mathbf{D}_t^C(\mathbf{p}_t) \mathbf{K}^{-1} \tilde{\mathbf{p}}_t \\ 1 \end{bmatrix}. \quad (10)$$

The relation between translational apparent motion and depth can then be written as follows:

$$\begin{aligned} \begin{bmatrix} {}^t\mathbf{F}_{t \rightarrow s}^O(\mathbf{p}_t) \\ \mathbf{0} \end{bmatrix} &= \frac{\mathbf{K} \begin{bmatrix} \mathbf{I} & \mathbf{t} \end{bmatrix} \begin{bmatrix} \mathbf{D}_t^C(\mathbf{p}_t) \mathbf{K}^{-1} \tilde{\mathbf{p}}_t \\ 1 \end{bmatrix}}{\mathbf{D}_s^C(\mathbf{p}_s)} - \tilde{\mathbf{p}}_t \quad (11) \\ &= \left( \frac{\mathbf{D}_t^C(\mathbf{p}_t)}{\mathbf{D}_s^C(\mathbf{p}_s)} - 1 \right) \tilde{\mathbf{p}}_t - \frac{\mathbf{K}\mathbf{t}}{\mathbf{D}_s^C(\mathbf{p}_s)} \\ &= \frac{t_3}{\mathbf{D}_s^C(\mathbf{p}_s)} \left( \tilde{\mathbf{p}}_t - \tilde{\mathbf{p}}_o - \mathbf{K} \begin{bmatrix} t_1/t_3 \\ t_2/t_3 \\ 0 \end{bmatrix} \right), \end{aligned}$$

where  $\mathbf{D}_s^C(\mathbf{p}_s) = \mathbf{D}_t^C(\mathbf{p}_t) - t_3$  under the condition of  $\mathbf{R} = \mathbf{I}$ , and  $\tilde{\mathbf{p}}_o$  denotes the homogeneous coordinates of the image principal point. We calculate the divergence of the optical flow at  $\mathbf{p}_t$  as follows:

$$\begin{aligned} \nabla \cdot {}^t\mathbf{F}_{t \rightarrow s}^O(\mathbf{p}_t) &= \nabla \cdot \left( \frac{t_3}{\mathbf{D}_t^C(\mathbf{p}_t) - t_3} \mathbf{q}_t \right) \\ &= \mathbf{q}_t \cdot \nabla \frac{t_3}{\mathbf{D}_t^C(\mathbf{p}_t) - t_3} + \frac{t_3}{\mathbf{D}_t^C(\mathbf{p}_t) - t_3} \nabla \cdot \mathbf{p}_t, \quad (12) \end{aligned}$$

where  $\nabla = [\frac{\partial}{\partial u}, \frac{\partial}{\partial v}]^\top$ , and  $\mathbf{q}_t$  is expressed as follows:

$$\begin{bmatrix} \mathbf{q}_t \\ 0 \end{bmatrix} = \tilde{\mathbf{p}}_t - \tilde{\mathbf{p}}_o - \mathbf{K} \begin{bmatrix} t_1/t_3 \\ t_2/t_3 \\ 0 \end{bmatrix}. \quad (13)$$

Rewriting (12) into the following expression:

$$\begin{aligned} &\underbrace{\frac{\mathbf{D}_t^C(\mathbf{p}_t) - t_3}{t_3} \nabla \cdot {}^t\mathbf{F}_{t \rightarrow s}^O(\mathbf{p}_t) - \nabla \cdot \mathbf{p}_t}_{\mathbf{C}^F(\mathbf{p}_t)} \\ &= - \underbrace{\frac{\mathbf{q}_t}{\mathbf{D}_t^C(\mathbf{p}_t) - t_3} \cdot \nabla \mathbf{D}_t^C(\mathbf{p}_t)}_{\mathbf{C}^D(\mathbf{p}_t)}. \quad (14) \end{aligned}$$

where  $\mathbf{C}^{F,D} \in \mathbb{R}^{H \times W}$  denotes the differential properties derived from optical flow divergence and depth gradient, respectively. This explicit relationship can be used to provide an additional constraint that helps further improve depth quality from the aspect of local variations via the following DPC loss:

$$\mathcal{L}_d = \frac{1}{HW} \sum_{\mathbf{p}} \frac{|\mathbf{C}^D(\mathbf{p}) - \mathbf{C}^F(\mathbf{p})|}{|\mathbf{C}^D(\mathbf{p})|}. \quad (15)$$

Similar to (7), we consider the relative error in (15). The effectiveness of our proposed DPC loss is validated through an ablation study detailed in Sect. IV-E.

TABLE I: Quantitative comparison with SoTA networks on the KITTI [45] dataset. The best results are shown in bold symbol. The symbols  $\uparrow$  and  $\downarrow$  indicate that higher and lower values correspond to better performance, respectively. ‘‘M’’ denotes training with monocular video sequences.

Method	Year	Resolution (pixels)	Data	Abs Rel $\downarrow$	Sq Rel $\downarrow$	RMSE $\downarrow$	RMSE log $\downarrow$	$\delta < 1.25 \uparrow$	$\delta < 1.25^2 \uparrow$	$\delta < 1.25^3 \uparrow$
Monodepth2 [10]	2019	192 $\times$ 640	M	0.115	0.903	4.863	0.193	0.877	0.959	0.981
HR-Depth [43]	2020	192 $\times$ 640	M	0.109	0.792	4.632	0.185	0.884	0.962	0.983
DIFFNet [8]	2021	192 $\times$ 640	M	0.102	0.764	4.483	0.180	0.890	0.964	0.983
MonoViT-tiny [9]	2022	192 $\times$ 640	M	0.102	0.733	4.459	0.177	0.895	0.965	0.984
Swin-Depth [46]	2023	192 $\times$ 640	M	0.106	0.739	4.510	0.182	0.890	0.964	0.984
Lite-Mono [14]	2023	192 $\times$ 640	M	0.107	0.765	4.561	0.183	0.886	0.963	0.983
Lite-Mono-8M [14]	2023	192 $\times$ 640	M	0.101	0.729	4.454	0.178	0.897	0.965	0.983
Dynamo-Depth [47]	2023	192 $\times$ 640	M	0.112	0.758	4.505	0.183	0.873	0.959	0.984
DaCCN [35]	2023	192 $\times$ 640	M	0.099	0.661	4.316	0.173	0.897	0.967	0.985
SENSE [48]	2023	192 $\times$ 640	M	0.104	0.693	4.294	0.177	0.894	0.965	0.984
AQUANet [49]	2024	192 $\times$ 640	M	0.105	<b>0.621</b>	<b>4.227</b>	0.179	0.889	0.964	0.984
<b>DCPI-Depth (Ours)</b>	-	192 $\times$ 640	M	<b>0.095</b>	0.662	4.274	<b>0.170</b>	<b>0.902</b>	<b>0.967</b>	<b>0.985</b>
Monodepth2 [10]	2019	320 $\times$ 1024	M	0.115	0.882	4.701	0.190	0.879	0.961	0.982
HR-Depth [43]	2020	320 $\times$ 1024	M	0.106	0.755	4.472	0.181	0.892	0.966	0.984
DIFFNet [8]	2021	320 $\times$ 1024	M	0.097	0.722	4.435	0.174	0.907	0.967	0.984
MonoViT-tiny [9]	2022	320 $\times$ 1024	M	0.096	0.714	4.292	0.172	0.908	0.968	0.984
DaCCN [35]	2023	320 $\times$ 1024	M	0.094	0.624	4.145	0.169	0.909	<b>0.970</b>	<b>0.985</b>
SENSE [48]	2023	320 $\times$ 1024	M	0.099	<b>0.617</b>	<b>4.079</b>	0.172	0.902	0.968	<b>0.985</b>
<b>DCPI-Depth (Ours)</b>	-	320 $\times$ 1024	M	<b>0.090</b>	0.655	4.113	<b>0.167</b>	<b>0.914</b>	0.969	<b>0.985</b>

#### D. Bidirectional Stream Co-Adjustment Strategy

In the conventional PCG stream, rigid flow is generated using the outputs from DepthNet and PoseNet, which are indirectly supervised by minimizing the photometric loss. DepthNet, when trained in this manner, often struggles in texture-less regions, where a pixel in the target video frame might correspond to multiple pixels with similar intensities in the source frame. Therefore, we are motivated to improve depth estimation in these regions by leveraging the dense correspondences provided by a well-trained FlowNet.

In our proposed CPG stream, despite the effectiveness of infusing dense correspondence priors provided by a pre-trained FlowNet into monocular depth estimation through our developed CGDC and DPC losses, these priors often capture independent apparent motions unrelated to depth when dynamic objects are involved. This can mislead DepthNet, resulting from inaccurately triangulated depths and the misalignment between optical flow divergence and depth gradient on such objects. A straightforward solution to this issue is to exclude dynamic regions using the auto-masking technique developed in [10] when computing CGDC and DPC losses. Nonetheless, as illustrated in Fig. 2(c), this technique is not sufficiently robust, as only the dynamic objects that are relatively stationary with respect to ego-motion can be effectively masked [10], and static regions, especially those with low texture, tend to be overly masked [49].

To address the aforementioned two challenges simultaneously, we propose a simple yet effective BSCA strategy, in which the PCG stream and CPG stream complement each other. We unfreeze the pre-trained FlowNet during training and jointly optimize the optical flow estimated in the CPG

stream and the rigid flow generated in the PCG stream by minimizing the following loss function:

$$\mathcal{L}_b = \frac{1}{HW} \sum_{\mathbf{p}} \frac{\left\| \mathbf{F}_{t \rightarrow s}^R(\mathbf{p}) - \mathbf{F}_{t \rightarrow s}^O(\mathbf{p}) \right\|_1}{\left\| \mathbf{F}_{t \rightarrow s}^O(\mathbf{p}) \right\|_1}. \quad (16)$$

In static regions, where optical flow and rigid flow should ideally be identical, (16) allows both flows to co-adjust without compromising photometric consistency and encourages rigid flow towards more accurate correspondences. On the other hand, in dynamic regions where optical flow and rigid flow differ significantly, (16) encourages the unfrozen FlowNet to generate ‘‘quasi’’ rigid flow, eliminating independent apparent motions that can mislead DepthNet, thereby retaining only the apparent motions consistent with the static scene hypothesis. This enables our CGDC and DPC losses to be effectively applied across the entire image, irrespective of static and dynamic regions. The generated ‘‘quasi’’ rigid flow produced by the adjusted FlowNet can, in turn, optimize depth estimation in dynamic regions via our developed CGDC and DPC losses. We conduct an ablation study in Sect. IV-E to demonstrate the effectiveness of this strategy.

## IV. EXPERIMENTS

The performance of our proposed DCPI-Depth is evaluated both qualitatively and quantitatively with extensive experiments in this section. The following subsections provide details on the utilized datasets, practical implementation, evaluation metrics, ablation studies, and comprehensive comparisons with other SoTA methods.

TABLE II: Quantitative comparison with SoTA networks on the KITTI [45] dataset using the improved KITTI ground truth provided in [50]. The best results are shown in bold symbol. The symbols  $\uparrow$  and  $\downarrow$  indicate that higher and lower values correspond to better performance, respectively. “M” denotes training with monocular video sequences, and “MS” denotes training with both monocular video sequences and stereo image pairs.  $\dagger$  indicates the results achieved using the same weights in Table I for consistency.

Method	Year	Resolution (pixels)	Data	Abs Rel $\downarrow$	Sq Rel $\downarrow$	RMSE $\downarrow$	RMSE log $\downarrow$	$\delta < 1.25 \uparrow$	$\delta < 1.25^2 \uparrow$	$\delta < 1.25^3 \uparrow$
Monodepth2 [10]	2019	192 × 640	MS	0.080	0.466	3.681	0.127	0.926	0.985	0.995
PackNet-SfM [31]	2020	192 × 640	M	0.078	0.420	3.485	0.121	0.931	0.986	0.996
CADepth [51]	2021	192 × 640	M	0.080	0.442	3.639	0.124	0.927	0.986	0.996
DIFFNet $\dagger$ [8]	2021	192 × 640	M	0.076	0.414	3.492	0.119	0.936	0.988	0.996
Lite-Mono $\dagger$ [14]	2023	192 × 640	M	0.077	0.413	3.482	0.119	0.933	0.988	0.997
Lite-Mono-8M $\dagger$ [14]	2023	192 × 640	M	0.077	0.423	3.527	0.119	0.934	0.988	0.997
SENSE [48]	2023	192 × 640	M	0.071	0.339	3.175	0.109	0.945	0.990	<b>0.998</b>
AQUANet [49]	2024	192 × 640	M	0.070	<b>0.285</b>	<b>2.988</b>	<b>0.107</b>	0.948	<b>0.992</b>	<b>0.998</b>
<b>DCPI-Depth<math>\dagger</math> (Ours)</b>	-	192 × 640	M	<b>0.066</b>	0.326	3.257	<b>0.107</b>	<b>0.949</b>	0.990	0.997

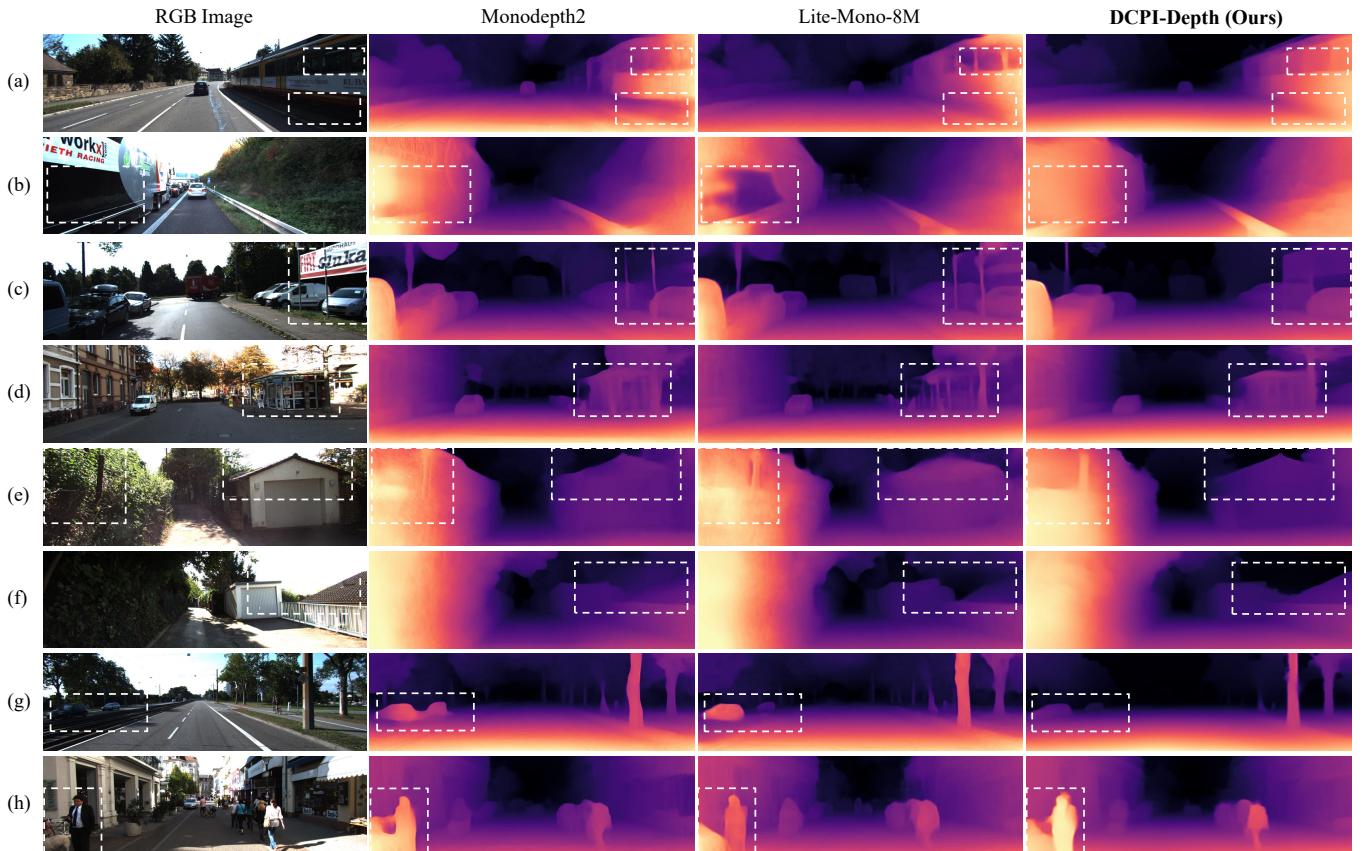


Fig. 3: Qualitative comparisons among Monodepth2, Lite-Mono-8M, and our proposed DCPI-Depth on the KITTI [45] dataset. (a)-(b), (c)-(d), (e)-(f), and (g)-(h) demonstrate the robustness of DCPI-Depth in texture-less regions, in texture-rich regions, at static object boundaries, and on dynamic objects, respectively.

#### A. Datasets

The **KITTI** [45] dataset contains 56 different scenes, evenly divided for model training and evaluation. Well-rectified stereo image pairs with depth information acquired from the LiDAR point clouds are provided. In our experiments, we adopt the Eigen split [5], which comprises 39,180 monocular triplets for training, 4,424 images for validation, and 697 images for

testing.

The **DDAD** [31] dataset consists of 200 urban driving scene sequences, with LiDAR point clouds provided to generate sparse ground-truth depth for model performance evaluation. Following [13], we split the dataset into a training set of 12,650 images and a test set of 3,950 images. As optical flow ground truth is unavailable in this dataset, we use FlowNet pre-trained on the KITTI dataset to provide dense correspondence

TABLE III: Quantitative results on the KITTI [45] dataset for the full image, static regions, and dynamic regions. The best results are shown in bold symbol. The symbols  $\uparrow$  and  $\downarrow$  indicate that higher and lower values correspond to better performance, respectively. “M” denotes training with monocular video sequences.

Region	Method	Year	Resolution (pixels)	Data	Abs Rel $\downarrow$	Sq Rel $\downarrow$	RMSE $\downarrow$	RMSE log $\downarrow$	$\delta < 1.25 \uparrow$	$\delta < 1.25^2 \uparrow$	$\delta < 1.25^3 \uparrow$
Full Image	SC-Depth [41]	2021	256 $\times$ 832	M	0.118	0.870	4.997	0.197	0.860	0.956	0.981
	SC-DepthV2 [44]	2022	256 $\times$ 832	M	0.118	0.861	4.803	0.193	0.866	0.958	0.981
	SC-DepthV3 [13]	2023	256 $\times$ 832	M	0.118	0.756	4.709	0.188	0.864	0.960	0.984
	<b>DCPI-Depth (Ours)</b>	-	256 $\times$ 832	M	<b>0.109</b>	<b>0.679</b>	<b>4.496</b>	<b>0.180</b>	<b>0.878</b>	<b>0.965</b>	<b>0.985</b>
Static Regions	SC-Depth [41]	2021	256 $\times$ 832	M	0.106	0.704	4.702	0.170	0.874	0.966	0.989
	SC-DepthV3 [13]	2023	256 $\times$ 832	M	0.108	0.636	4.438	0.163	0.881	0.971	0.991
	<b>DCPI-Depth (Ours)</b>	-	256 $\times$ 832	M	<b>0.101</b>	<b>0.584</b>	<b>4.235</b>	<b>0.156</b>	<b>0.892</b>	<b>0.974</b>	<b>0.991</b>
Dynamic Regions	SC-Depth [41]	2021	256 $\times$ 832	M	0.243	3.890	8.533	0.321	0.689	0.849	0.921
	SC-DepthV3 [13]	2023	256 $\times$ 832	M	0.205	2.283	7.356	0.290	0.703	0.884	0.945
	<b>DCPI-Depth (Ours)</b>	-	256 $\times$ 832	M	<b>0.186</b>	<b>1.948</b>	<b>7.028</b>	<b>0.281</b>	<b>0.732</b>	<b>0.895</b>	<b>0.950</b>

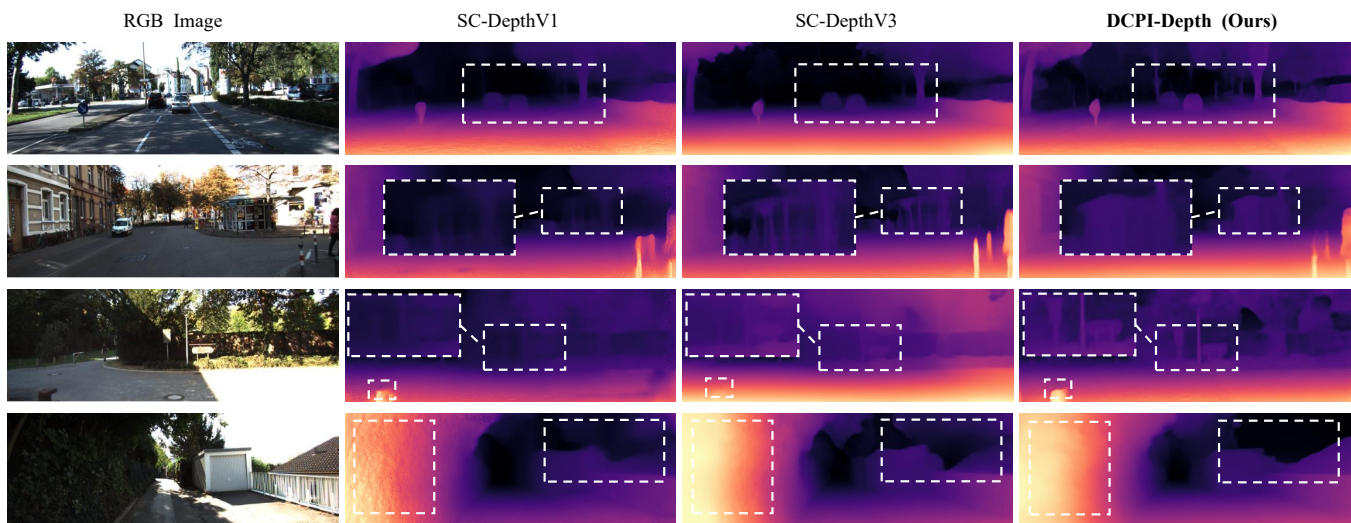


Fig. 4: Qualitative comparison among SC-DepthV1, SC-DepthV3, and our DCPI-Depth on the KITTI [45] dataset.

priors.

The **Make3D** [52] dataset contains 134 images of outdoor scenes along with their corresponding depth maps. Since neither stereo image pairs nor monocular sequences are provided, we cannot use this dataset to train monocular depth estimation networks in a unsupervised manner. Therefore, we only use this dataset to quantify the generalizability of models pre-trained on the KITTI dataset.

### B. Experimental Setup

Our experiments are conducted on an NVIDIA RTX 4090 GPU with a batch size of 12. Following [10], we adopt a training approach wherein a snippet of three consecutive video frames is utilized as a training sample. To augment the dataset, random color jitter and horizontal flips are applied to the images during model training. We use AdamW [53] optimizer to minimize the loss functions, and train the network for 30 epochs with an initial learning rate of  $10^{-4}$  and a weight decay of  $10^{-2}$ . Following [10], [14], the network’s encoder is initialized using pre-trained weights from the ImageNet

database [54]. RAFT [17], a highly efficient optical flow estimation network pre-trained on the KITTI Flow 2015 dataset, is employed as the FlowNet in our framework to provide dense correspondence prior.

### C. Evaluation Metrics

We employ seven metrics to quantify the model’s performance: mean absolute relative error (Abs Rel), mean squared relative error (Sq Rel), root mean squared error (RMSE), root mean squared log error (RMSE log), and the accuracy under specific thresholds ( $\delta_i < 1.25^i$ , where  $i = 1, 2, 3$ ). Detailed expressions for these metrics can be found in [5].

### D. Comparison with SoTA Approaches

The quantitative experimental results presented in Table I demonstrate that DCPI-Depth achieves SoTA performance when processing images with resolutions of  $192 \times 640$  pixels and  $320 \times 1024$  pixels. Specifically, our DCPI-Depth outperforms all other SoTA un/self-supervised methods, achieving a 4.0% reduction in Abs Rel and a 0.6% improvement in  $\delta_1$  at



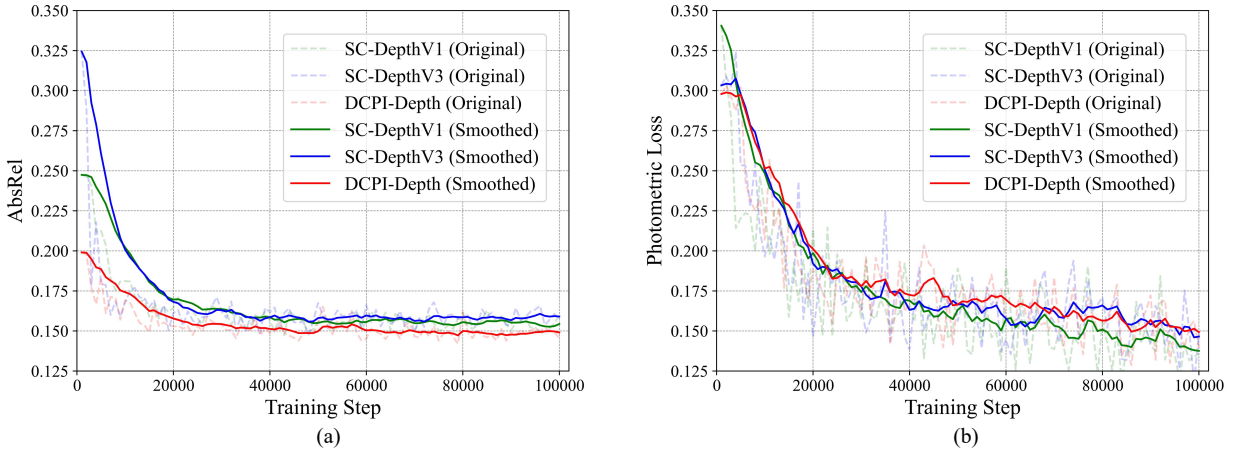


Fig. 5: Learning curve comparisons among SC-DepthV1, SC-DepthV3, and our proposed DCPI-Depth on the KITTI [45] dataset: (a) demonstrates that our DCPI-Depth consistently achieves a lower Abs Rel throughout training compared to other models; (b) illustrates that the convergence of photometric loss among the three models is comparable.

TABLE IV: Ablation studies on the KITTI [45] dataset. The best results are shown in bold symbol. The symbols  $\uparrow$  and  $\downarrow$  indicate that higher and lower values correspond to better performance, respectively.

DepthNet	CPG Stream		BSCA Strategy	Full Image					Static Regions			Dynamic Regions		
	CGDC loss	DPC loss		Abs Rel $\downarrow$	Sq Rel $\downarrow$	RMSE $\downarrow$	$\delta_1 \uparrow$	$\delta_2 \uparrow$	Abs Rel $\downarrow$	Sq Rel $\downarrow$	$\delta_1 \uparrow$	Abs Rel $\downarrow$	Sq Rel $\downarrow$	$\delta_1 \uparrow$
ResNet18 [55]	Baseline			0.118	0.756	4.709	0.864	0.960	0.108	0.636	0.881	0.205	2.283	0.703
	✓		✓	0.111	0.698	4.584	0.874	0.963	0.103	0.601	0.888	0.193	2.125	0.718
		✓	✓	0.115	0.716	4.611	0.869	0.963	0.105	0.610	0.886	0.201	2.234	0.710
	✓	✓		0.113	0.707	4.559	0.873	0.964	0.103	0.591	0.891	0.211	2.510	0.700
	✓	✓	✓	<b>0.109</b>	<b>0.679</b>	<b>4.496</b>	<b>0.878</b>	<b>0.965</b>	<b>0.101</b>	<b>0.584</b>	<b>0.892</b>	<b>0.186</b>	<b>1.948</b>	<b>0.732</b>
DIFFNet [8]	Baseline			0.108	0.696	4.591	0.878	0.964	0.099	0.603	0.892	0.197	2.188	0.717
	✓	✓	✓	<b>0.103</b>	<b>0.653</b>	<b>4.483</b>	<b>0.886</b>	<b>0.966</b>	<b>0.094</b>	<b>0.555</b>	<b>0.900</b>	<b>0.191</b>	<b>2.098</b>	<b>0.719</b>

a resolution is  $192 \times 640$  pixels. Given the known limitations of the ground truth quality in the KITTI dataset, we further evaluate our network performance using the KITTI improved ground truth [50]. It can be observed in Table II that DCPI-Depth consistently outperforms the previous SoTA method [35] across all metrics.

The qualitative experimental results on the KITTI dataset are shown in Fig. 3. Our DCPI-Depth exhibits superior performance compared to previous SoTA methods. This is particularly evident in texture-less regions, such as (a) and (b). Additionally, our approach ensures smoother and more continuous depth changes and generates clearer boundaries, as exemplified in (c) to (f). These improvements are attributed to the dense correspondence priors infused via our proposed CGDC and DPC losses within the CPG stream, which provide refined and direct geometric cues for depth estimation. Furthermore, DCPI-Depth maintains accurate depth estimation on dynamic objects, such as (g) and (h), unaffected by independent motion. This advantage, observed on dynamic objects, stems from our BSCA strategy, which not only prevents the misleading effects of independent motion captured by the optical flow within the CPG stream but also reinforces accurate estimations early in the training phase, preserving them through to the final results.

To further validate the effectiveness of DCPI-Depth in leveraging dense correspondence priors, we deploy our framework to SC-DepthV3 [13], which leverages pseudo depth to achieve robust and highly reliable depth estimation. It also provides a comprehensive platform for evaluating depth performance across dynamic objects, static areas, and full images. As shown in Table III, DCPI-Depth achieves significant improvements, outperforming the baseline by a considerable margin across all metrics for full image, static regions, and dynamic regions. Furthermore, we provide comparisons of learning curves among SC-DepthV1, SC-DepthV3, and DCPI-Depth. As illustrated in Fig. 5(a), DCPI-Depth significantly improves depth estimation performance compared to SC-DepthV3. These results demonstrate that the dense correspondence prior we incorporate additionally provides meaningful geometric cues on top of pseudo depth. Moreover, it can be observed in Fig. 5(b) that the convergence of the photometric loss is comparable among the three models. This observation suggests that merely minimizing photometric loss, which provides an indirect supervisory signal, presents challenges in further improving depth estimation performance. In contrast, our approach provides a more direct and effective constraint for depth estimation. The qualitative results shown

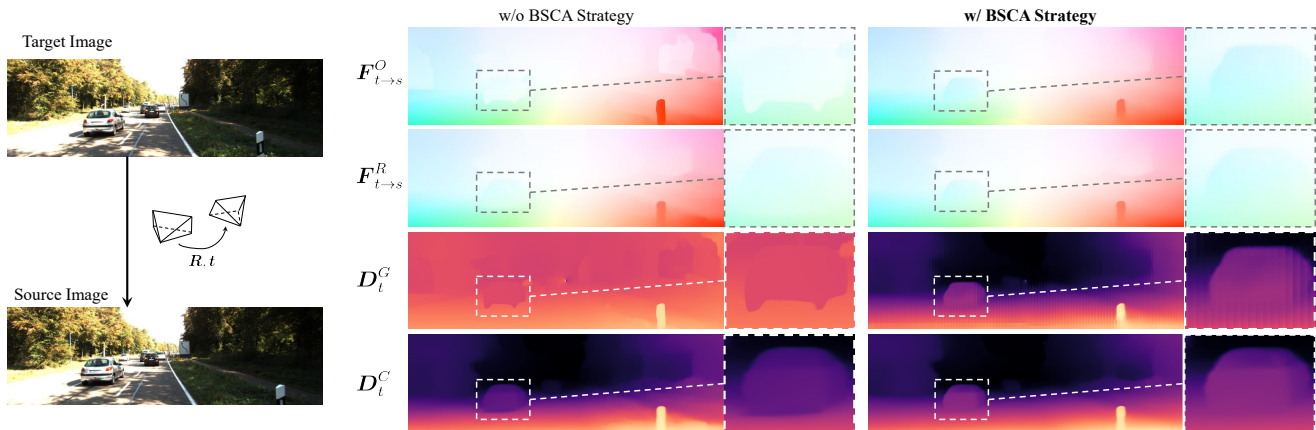


Fig. 6: Qualitative results on the KITTI [45] dataset to demonstrate the effectiveness of the BSCA strategy.

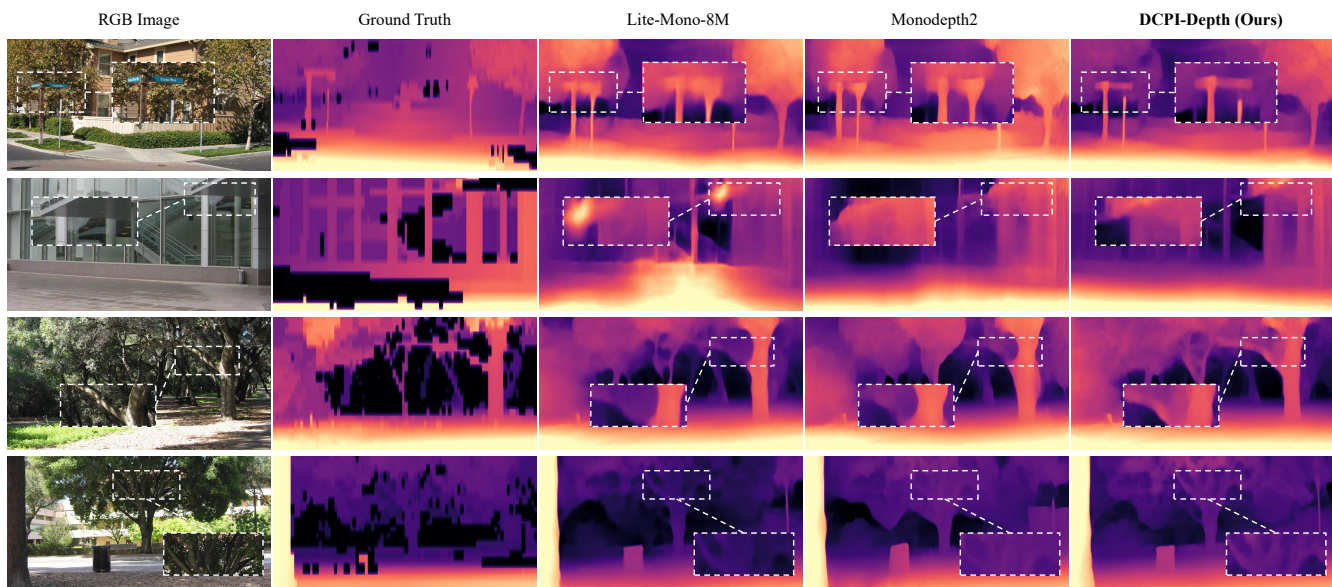


Fig. 7: Qualitative zero-shot monocular depth estimation results on the Make3D [52] dataset.

in Fig. 4 also indicate that DCPI-Depth excels, particularly in preserving clear object boundaries and maintaining robustness in ambiguous regions. This validates the effectiveness of incorporating dense correspondence priors into depth estimation frameworks.

### E. Ablation Studies

Table IV and V presents comprehensive ablation studies conducted with SC-DepthV3 to validate the effectiveness of our contributed components. The first ablation study validates the internal design of the CPG stream by comparing the overall performance with and without the incorporation of the CGDC loss and DPC loss, respectively. Key findings from this study include: (1) employing either the CGDC loss or the DPC loss independently leads to improved performance; (2) the combined use of both losses leads to more substantial improvements compared to using each loss individually.

Additionally, we conduct another ablation study where we omit the BSCA strategy while retaining the full configuration

of the CPG stream to validate its efficacy. The quantitative results reveal a significant decline in performance in dynamic regions, even falling below that of the baseline network, while the depth estimation accuracy in static regions remains unaffected. The qualitative results are provided in Fig. 6. It can be observed that the moving car exhibits independent apparent motions in the optical flow provided by the frozen FlowNet, leading to erroneous depth guidance via triangulation. As a result, the rigid flow eventually tends to contain the independent apparent motions, and the estimated depth is farther than the actual. In contrast, the model trained with the BSCA strategy effectively eliminates independent apparent motions in both flows for the moving car. This results in more accurate geometric and contextual-based depth estimations for the moving car. The above observations are consistent with our initial motivation for introducing the BSCA strategy, emphasizing its critical role in improving depth estimation performance when dynamic objects are involved.

Thirdly, we conduct an ablation study using a better-

TABLE V: Ablation study to demonstrate the effectiveness of our approach with respect to different dense correspondence prior qualities on the KITTI [45] dataset. ‘‘F1-EPE’’ (pixels) and ‘‘F1-All’’ (pixels) are two metrics used to quantify the performance of FlowNet, where lower values indicate better performance.

Pre-trained FlowNet	Optical Flow Quality		Depth Estimation Metrics				
	F1-EPE	F1-All	Abs Rel	Sq Rel	RMSE	$\delta_1$	$\delta_2$
w/	<b>0.63</b>	<b>1.50</b>	<b>0.109</b>	<b>0.679</b>	<b>4.496</b>	<b>0.878</b>	<b>0.965</b>
w/	1.94	9.83	0.113	0.695	4.640	0.871	0.963
w/o	-	-	0.118	0.756	4.709	0.864	0.960

TABLE VI: Quantitative experimental results for SoTA monocular depth estimation models, with and without our proposed DCPI-Depth framework employed, using the KITTI Eigen split [5]. All models are trained on  $192 \times 640$  images.

Method	Abs Rel	Sq Rel	RMSE	RMSE log	$\delta_1$	$\delta_2$	$\delta_3$
Monodepth2 [10]	0.115	0.903	4.863	0.193	0.877	0.959	0.981
<b>+Ours</b>	<b>0.110</b>	<b>0.749</b>	<b>4.559</b>	<b>0.183</b>	<b>0.879</b>	<b>0.962</b>	<b>0.984</b>
Swin-Depth [46]	0.106	0.739	4.510	0.182	0.890	0.964	0.984
<b>+Ours</b>	<b>0.104</b>	<b>0.704</b>	<b>4.443</b>	<b>0.180</b>	<b>0.893</b>	<b>0.965</b>	0.984
DIFFNet [8]	0.102	0.764	4.483	0.180	0.896	0.965	0.983
<b>+Ours</b>	<b>0.096</b>	<b>0.670</b>	<b>4.310</b>	<b>0.172</b>	<b>0.901</b>	<b>0.966</b>	<b>0.984</b>
Lite-Mono [14]	0.107	0.765	4.561	0.183	0.886	0.963	0.983
<b>+Ours</b>	<b>0.101</b>	<b>0.707</b>	<b>4.447</b>	<b>0.176</b>	<b>0.893</b>	<b>0.964</b>	<b>0.984</b>
Lite-Mono-8M [14]	0.101	0.729	4.454	0.178	0.897	0.965	0.983
<b>+Ours</b>	<b>0.095</b>	<b>0.662</b>	<b>4.274</b>	<b>0.170</b>	<b>0.902</b>	<b>0.967</b>	<b>0.985</b>

performing DepthNet backbone within our full configuration. The results show that our contributed techniques are compatible with this backbone and consistently achieve significant improvements. These findings indicate that our contributions provide distinct advantages that differentiate them from those provided by more advanced networks and demonstrate the potential to deliver improvements across a wider range of models.

Finally, as shown in Table V, we evaluate the performance of our approach with respect to different qualities of dense correspondence priors. These results suggest the robustness of our method, demonstrating effective performance even when the dense correspondences are of low quality (when FlowNet is trained with an insufficient number of iterations). We attribute this phenomenon to the fact that even low-quality dense correspondence priors can provide valuable guidance for training DepthNet, helping perceive relative distances among pixels and reflecting depth variations to some extent. Meanwhile, this also benefits from our BSCA strategy, which effectively allows the two types of flows to complement each other.

#### F. Generalizability Evaluation

We incorporate the CPG stream and the BSCA strategy into existing open-source methods to further demonstrate the

TABLE VII: Quantitative results on the DDAD [31] dataset.

Method	Abs Rel	Sq Rel	RMSE	RMSE log	$\delta_1$	$\delta_2$	$\delta_3$
SC-DepthV1	0.169	3.877	16.290	0.280	0.773	0.905	0.951
SC-DepthV3	<b>0.142</b>	3.031	15.868	0.248	<b>0.813</b>	0.922	0.963
<b>DCPI-Depth (Ours)</b>	0.143	<b>2.963</b>	<b>15.380</b>	<b>0.244</b>	0.812	<b>0.925</b>	<b>0.966</b>

TABLE VIII: Quantitative results on the Make3D [52] dataset. All models are trained on the KITTI [45] dataset images (resolution:  $640 \times 192$  pixels).

Method	Abs Rel	Sq Rel	RMSE	RMSE log
Monodepth2 [10]	0.321	3.378	7.252	0.163
HR-Depth [43]	0.305	2.944	6.857	0.157
CADepth [51]	0.319	3.564	7.152	0.158
R-MSFM6 [51]	0.334	3.285	7.212	0.169
Lite-Mono-8M [14]	0.305	3.060	6.981	0.158
<b>DCPI-Depth (Ours)</b>	<b>0.291</b>	<b>2.944</b>	<b>6.817</b>	<b>0.150</b>

adaptability of our contributions to other SoTA methods. As shown in Table VI, our proposed stream and strategy significantly improve the performance of the original networks across all metrics, which consistently validates the scalability of our methods, as detailed in Sect. IV-E.

In addition, we employ FlowNet, pre-trained on the KITTI Flow 2015 [56] dataset, within our DCPI-Depth framework, and train our model on the DDAD [31] dataset to evaluate the generalizability of the dense correspondence prior provided by the pre-trained FlowNet. The results presented in Table VII indicate that our method improves the depth estimation performance across five metrics. However, the improvements are not as significant as those observed when trained on the KITTI dataset. This limitation may be due to the domain gap between these two datasets.

Finally, we conduct a zero-shot experiment on the Make3D [52] dataset using the pre-trained weights from KITTI. As shown in Table VIII and Fig. 7, our model outperforms all other methods, demonstrating its ability to generalize effectively to new, unseen scenes.

## V. CONCLUSION

This article presented DCPI-Depth, a novel unsupervised monocular depth estimation framework with two bidirectional and collaborative streams: a conventional PCG stream and a newly developed CPG stream. The latter was designed specifically to infuse dense correspondence priors into monocular depth estimation. It consists of a CGDC loss to provide contextual-based depth with geometric guidance obtained from ego-motion and dense correspondence priors, and a DPC loss to constrain the local depth variation using the explicit relationship between the differential properties of depth and optical flow. Moreover, a BSCA strategy was developed to enhance the interaction between the two flow types, encouraging the rigid flow towards more accurate correspondence and making the optical flow more adaptable across various scenarios under

the static scene hypotheses. Compared to previous works, our DCPI-Depth framework has demonstrated impressive performance and superior generalizability on the KITTI, DDAD, and Make3D datasets. Future work will focus on exploring more advanced optical flow estimation techniques to enhance the reliability and generalizability of dense correspondence priors and to extend the techniques in DCPI-Depth into a joint learning framework where multiple tasks can explicitly couple and mutually enhance each other.

## REFERENCES

- [1] A. Geiger *et al.*, “Vision meets robotics: The KITTI dataset,” *The International Journal of Robotics Research*, vol. 32, no. 11, pp. 1231–1237, 2013.
- [2] X. Luo *et al.*, “Consistent video depth estimation,” *ACM Transactions on Graphics*, vol. 39, no. 4, pp. 71–1, 2020.
- [3] W. Wang *et al.*, “Visual robotic manipulation with depth-aware pretraining,” *arXiv preprint arXiv:2401.09038*, 2024.
- [4] T. Zhou *et al.*, “Unsupervised learning of depth and ego-motion from video,” in *Proceedings of the IEEE/CVF Conference on Computer Vision and Pattern Recognition (CVPR)*, 2017, pp. 1851–1858.
- [5] D. Eigen *et al.*, “Depth map prediction from a single image using a multi-scale deep network,” *Advances in Neural Information Processing Systems (NeurIPS)*, vol. 27, 2014.
- [6] F. Liu *et al.*, “Learning depth from single monocular images using deep convolutional neural fields,” *IEEE Transactions on Pattern Analysis and Machine Intelligence*, vol. 38, no. 10, pp. 2024–2039, 2015.
- [7] M. Song *et al.*, “Monocular depth estimation using laplacian pyramid-based depth residuals,” *IEEE Transactions on Circuits and Systems for Video Technology*, vol. 31, no. 11, pp. 4381–4393, 2021.
- [8] H. Zhou *et al.*, “Self-supervised monocular depth estimation with internal feature fusion,” *arXiv preprint arXiv:2110.09482*, 2021.
- [9] C. Zhao *et al.*, “MonoViT: Self-supervised monocular depth estimation with a vision transformer,” in *2022 International Conference on 3D Vision (3DV)*. IEEE, 2022, pp. 668–678.
- [10] C. Godard *et al.*, “Digging into self-supervised monocular depth estimation,” in *Proceedings of the IEEE/CVF International Conference on Computer Vision (ICCV)*, 2019, pp. 3828–3838.
- [11] X. Xu *et al.*, “Multi-scale spatial attention-guided monocular depth estimation with semantic enhancement,” *IEEE Transactions on Image Processing*, vol. 30, pp. 8811–8822, 2021.
- [12] X. Song *et al.*, “Unsupervised monocular estimation of depth and visual odometry using attention and depth-pose consistency loss,” *IEEE Transactions on Multimedia*, 2023.
- [13] L. Sun *et al.*, “SC-DepthV3: Robust self-supervised monocular depth estimation for dynamic scenes,” *IEEE Transactions on Pattern Analysis and Machine Intelligence*, vol. 46, no. 1, pp. 497–508, 2023.
- [14] N. Zhang *et al.*, “Lite-Mono: A lightweight CNN and Transformer architecture for self-supervised monocular depth estimation,” in *Proceedings of the IEEE/CVF Conference on Computer Vision and Pattern Recognition (CVPR)*, 2023, pp. 18 537–18 546.
- [15] C. Godard *et al.*, “Unsupervised monocular depth estimation with left-right consistency,” in *Proceedings of the IEEE/CVF Conference on Computer Vision and Pattern Recognition (CVPR)*, 2017, pp. 270–279.
- [16] X. Ye *et al.*, “Unsupervised monocular depth estimation via recursive stereo distillation,” *IEEE Transactions on Image Processing*, vol. 30, pp. 4492–4504, 2021.
- [17] Z. Teed and J. Deng, “RAFT: Recurrent all-pairs field transforms for optical flow,” in *Proceedings of the European Conference on Computer Vision (ECCV)*. Springer, 2020, pp. 402–419.
- [18] R. I. Hartley and P. Sturm, “Triangulation,” *Computer Vision and Image Understanding*, vol. 68, no. 2, pp. 146–157, 1997.
- [19] Y. Cao *et al.*, “Estimating depth from monocular images as classification using deep fully convolutional residual networks,” *IEEE Transactions on Circuits and Systems for Video Technology*, vol. 28, no. 11, pp. 3174–3182, 2017.
- [20] W. Yin *et al.*, “Enforcing geometric constraints of virtual normal for depth prediction,” in *Proceedings of the IEEE/CVF International Conference on Computer Vision (ICCV)*, 2019, pp. 5684–5693.
- [21] J. Hu *et al.*, “Revisiting single image depth estimation: Toward higher resolution maps with accurate object boundaries,” in *2019 IEEE Winter Conference on Applications of Computer Vision (WACV)*. IEEE, 2019, pp. 1043–1051.
- [22] H. Fu *et al.*, “Deep ordinal regression network for monocular depth estimation,” in *Proceedings of the IEEE/CVF Conference on Computer Vision and Pattern Recognition (CVPR)*, 2018, pp. 2002–2011.
- [23] S. F. Bhat *et al.*, “AdaBins: Depth estimation using adaptive bins,” in *Proceedings of the IEEE/CVF Conference on Computer Vision and Pattern Recognition (CVPR)*, 2021, pp. 4009–4018.
- [24] J. H. Lee *et al.*, “From big to small: Multi-scale local planar guidance for monocular depth estimation,” *arXiv preprint arXiv:1907.10326*, 2019.
- [25] G. Yang *et al.*, “Transformer-based attention networks for continuous pixel-wise prediction,” in *Proceedings of the IEEE/CVF International Conference on Computer Vision (ICCV)*, 2021, pp. 16 269–16 279.
- [26] L. Yang *et al.*, “Depth anything: Unleashing the power of large-scale unlabeled data,” *arXiv preprint arXiv:2401.10891*, 2024.
- [27] R. Birkl *et al.*, “Midas v3. 1—a model zoo for robust monocular relative depth estimation,” *arXiv preprint arXiv:2307.14460*, 2023.
- [28] M. Oquab *et al.*, “DINOv2: Learning robust visual features without supervision,” *Transactions on Machine Learning Research*, 2024. [Online]. Available: <https://openreview.net/forum?id=a68SUt6zFt>
- [29] R. Garg *et al.*, “Unsupervised cnn for single view depth estimation: Geometry to the rescue,” in *Proceedings of the European Conference on Computer Vision (ECCV)*. Springer, 2016, pp. 740–756.
- [30] Y. Zhang *et al.*, “Unsupervised multi-view constrained convolutional network for accurate depth estimation,” *IEEE Transactions on Image Processing*, vol. 29, pp. 7019–7031, 2020.
- [31] V. Guizilini *et al.*, “3D packing for self-supervised monocular depth estimation,” in *Proceedings of the IEEE/CVF Conference on Computer Vision and Pattern Recognition (CVPR)*, 2020, pp. 2485–2494.
- [32] X. Song *et al.*, “MLDA-Net: Multi-level dual attention-based network for self-supervised monocular depth estimation,” *IEEE Transactions on Image Processing*, vol. 30, pp. 4691–4705, 2021.
- [33] R. Peng *et al.*, “Excavating the potential capacity of self-supervised monocular depth estimation,” in *Proceedings of the IEEE/CVF International Conference on Computer Vision (ICCV)*, 2021, pp. 15 560–15 569.
- [34] Y. Zhang *et al.*, “Self-supervised monocular depth estimation with multiscale perception,” *IEEE Transactions on Image Processing*, vol. 31, pp. 3251–3266, 2022.
- [35] W. Han *et al.*, “Self-supervised monocular depth estimation by direction-aware cumulative convolution network,” in *Proceedings of the IEEE/CVF International Conference on Computer Vision (ICCV)*, 2023, pp. 8613–8623.
- [36] Z. Yin and J. Shi, “GeoNet: Unsupervised learning of dense depth, optical flow and camera pose,” in *Proceedings of the IEEE/CVF Conference on Computer Vision and Pattern Recognition (CVPR)*, 2018, pp. 1983–1992.
- [37] Y. Chen *et al.*, “Self-supervised learning with geometric constraints in monocular video: Connecting flow, depth, and camera,” in *Proceedings of the IEEE/CVF International Conference on Computer Vision (ICCV)*, 2019, pp. 7063–7072.
- [38] A. Ranjan *et al.*, “Competitive collaboration: Joint unsupervised learning of depth, camera motion, optical flow and motion segmentation,” in *Proceedings of the IEEE/CVF Conference on Computer Vision and Pattern Recognition (CVPR)*, 2019, pp. 12 240–12 249.
- [39] X. Chen *et al.*, “Self-supervised monocular depth estimation: Solving the edge-fattening problem,” in *Proceedings of the IEEE/CVF Winter Conference on Applications of Computer Vision (WACV)*, 2023, pp. 5776–5786.
- [40] H. Jung *et al.*, “Fine-grained semantics-aware representation enhancement for self-supervised monocular depth estimation,” in *Proceedings of the IEEE/CVF International Conference on Computer Vision (ICCV)*, 2021, pp. 12 642–12 652.
- [41] J.-W. Bian *et al.*, “Unsupervised scale-consistent depth learning from video,” *International Journal of Computer Vision*, vol. 129, no. 9, pp. 2548–2564, 2021.
- [42] Z. Wang *et al.*, “Image quality assessment: from error visibility to structural similarity,” *IEEE Transactions on Image Processing*, vol. 13, no. 4, pp. 600–612, 2004.
- [43] X. Lyu *et al.*, “HR-depth: High resolution self-supervised monocular depth estimation,” in *Proceedings of the AAAI Conference on Artificial Intelligence*, vol. 35, no. 3, 2021, pp. 2294–2301.
- [44] J.-W. Bian *et al.*, “Auto-rectify network for unsupervised indoor depth estimation,” *IEEE Transactions on Pattern Analysis and Machine Intelligence*, vol. 44, no. 12, pp. 9802–9813, 2021.
- [45] A. Geiger *et al.*, “Are we ready for autonomous driving? the KITTI vision benchmark suite,” in *Proceedings of the IEEE/CVF Conference on Computer Vision and Pattern Recognition (CVPR)*. IEEE, 2012, pp. 3354–3361.

- [46] D. Shim and H. J. Kim, "Swindepth: Unsupervised depth estimation using monocular sequences via swin transformer and densely cascaded network," in *Proceedings of the IEEE International Conference on Robotics and Automation (ICRA)*. IEEE, 2023, pp. 4983–4990.
- [47] Y. Sun and B. Hariharan, "Dynamo-Depth: Fixing unsupervised depth estimation for dynamical scenes," *Advances in Neural Information Processing Systems (NeurIPS)*, 2023.
- [48] G. Li *et al.*, "SENSE: Self-evolving learning for self-supervised monocular depth estimation," *IEEE Transactions on Image Processing*, 2023.
- [49] J. L. G. Bello *et al.*, "Self-supervised monocular depth estimation with positional shift depth variance and adaptive disparity quantization," *IEEE Transactions on Image Processing*, 2024.
- [50] J. Uhrig *et al.*, "Sparsity invariant CNNs," in *2017 International Conference on 3D Vision (3DV)*. IEEE, 2017, pp. 11–20.
- [51] J. Yan *et al.*, "Channel-wise attention-based network for self-supervised monocular depth estimation," in *2021 International Conference on 3D vision (3DV)*. IEEE, 2021, pp. 464–473.
- [52] A. Saxena *et al.*, "Make3D: Learning 3d scene structure from a single still image," *IEEE Transactions on Pattern Analysis and Machine Intelligence*, vol. 31, no. 5, pp. 824–840, 2008.
- [53] I. Loshchilov and F. Hutter, "Decoupled weight decay regularization," *arXiv preprint arXiv:1711.05101*, 2017.
- [54] J. Deng *et al.*, "ImageNet: A large-scale hierarchical image database," in *Proceedings of the IEEE/CVF Conference on Computer Vision and Pattern Recognition (CVPR)*. Ieee, 2009, pp. 248–255.
- [55] K. He *et al.*, "Deep residual learning for image recognition," in *Proceedings of the IEEE/CVF Conference on Computer Vision and Pattern Recognition (CVPR)*, 2016, pp. 770–778.
- [56] M. Menze and A. Geiger, "Object scene flow for autonomous vehicles," in *Proceedings of the IEEE/CVF Conference on Computer Vision and Pattern Recognition (CVPR)*, 2015, pp. 3061–3070.